


Tunable tunnel coupling in a double quantum antidot with cotunneling via localized state

Tokuro Hata¹, Kazuhiro Sada¹, Tomoki Uchino¹, Daisuke Endo¹, Takafumi Akiho²,
Koji Muraki² and Toshimasa Fujisawa¹

¹*Department of Physics, Tokyo Institute of Technology, 2-12-1 Ookayama, Meguro, Tokyo 152-8551, Japan*

²*NTT Basic Research Laboratories, 3-1 Morinosato Wakamiya, Atsugi-shi, Kanagawa 243-0198, Japan*

 (Received 28 February 2023; revised 27 July 2023; accepted 14 August 2023; published 28 August 2023)

Controlling tunnel coupling between quantum antidots (QADs) in the quantum Hall (QH) regime is problematic. We propose and demonstrate a scheme for tunable tunnel coupling between two QADs by utilizing a cotunneling process via a localized state as a third QAD. The effective tunnel coupling can be tuned by changing the localized level even with constant nearest-neighbor tunnel couplings. We systematically study the variation of transport characteristics in the effectively triple QAD system at the Landau level filling factor $\nu = 2$. The tunable tunnel coupling is clarified by analyzing the anticrossing of Coulomb blockade peaks in the charge stability diagram, in agreement with numerical simulations based on the master equation. The scheme is attractive for studying coherence and interaction in QH systems.

DOI: [10.1103/PhysRevB.108.075432](https://doi.org/10.1103/PhysRevB.108.075432)

I. INTRODUCTION

Controlling quantum coherence and interaction between particles is a central subject in mesoscopic physics of conventional and topological states of matter. In the case of the integer and fractional quantum Hall (QH) regimes, the interplay between the Aharonov-Bohm effect and the Coulomb blockade (CB) effect has been discussed for small filled regions [quantum dots (QDs)] [1–3] and small empty regions [quantum antidots (QADs)] [4–9]. Understanding the two effects is essential to unveil the anyon statistics of fractional charges [10–13]. Double QDs and QADs should provide another platform for better control of coherency and interaction. Particularly, double QADs allow us to study coherent tunneling of quasiparticles [14]. However, in contrast to the successful development of quantum information devices with QDs [15–17], controlling tunnel and electrostatic couplings in double QADs remains challenging even in the integer quantum Hall regime. While a few papers report on the tunnel and electrostatic coupling of double QADs, finite tunnel couplings are confirmed only at some particular conditions without tuning capability [18,19]. Tunable coupling strength is highly desirable for manipulating quasiparticles. The issue might be related to the formation of tunnel barriers in a QH insulator with a narrow energy gap determined by the cyclotron and Zeeman energies [20]. The barrier height cannot exceed the energy gap, and localized states randomly distributed in the QH insulator are unexpectedly charged or discharged. Smooth control of tunnel coupling may not be available with standard techniques.

Here, we propose a triple QAD configuration to control the tunnel coupling between the outer two QADs by using the second-order tunneling process through the central QAD. The basic characteristics are investigated by using a localized state acting as the central QAD located between well-controlled QADs with gates. The charge stability diagram shows a dramatic change from the parallelogram

pattern showing negligible coupling between the two QADs to the rounded honeycomb pattern manifesting the presence of tunnel coupling by controlling the energy level of the localized state. The transition is consistent with a model calculation involving the hybridization of the electronic states in the triple QAD. The scheme might be useful in studying coherent tunneling of quasiparticles in a controllable way.

II. TRIPLE QAD SYSTEM

We consider a triple QAD system at Landau level filling factor $\nu_B = 2$ in the bulk, as shown in Fig. 1(a). The left (L), central (C), and right (R) QADs are formed with local filling factors, $\nu_L = 0$, $\nu_C = 1$, and $\nu_R = 0$, respectively, between the source (S) and drain (D) regions, where $\nu_C = 1$ is assumed for a localized state as QAD C in this paper. The following scheme should work even for other filling factors. The energy diagram of the system is schematically shown in Fig. 1(b) for spin-up and -down branches of the lowest and second-lowest Landau levels. Transport is dominated by tunneling through bound states, ε_L , ε_C , and ε_R , in the spin-down lowest Landau level ($0\downarrow$). The tunnel coupling, t_{LC} and t_{CR} , and the electrostatic coupling, U_{LC} and U_{CR} , should be determined by the potential profile of the QH insulator. Notice that the bulk is insulating only near the QH filling factor ($\nu_B = 2$ in our case). Deviation from the integer value induces occupation of integer charges on localized states randomly distributed in the sample, which alters the potential profile. Therefore, standard techniques, such as surface gates that change the electron density underneath and adjusting magnetic field that changes the flux density, may not provide smooth control of tunnel coupling. Here, we use ε_C as a control knob to induce tunnel and electrostatic coupling between QADs L and R by utilizing second-order tunneling.

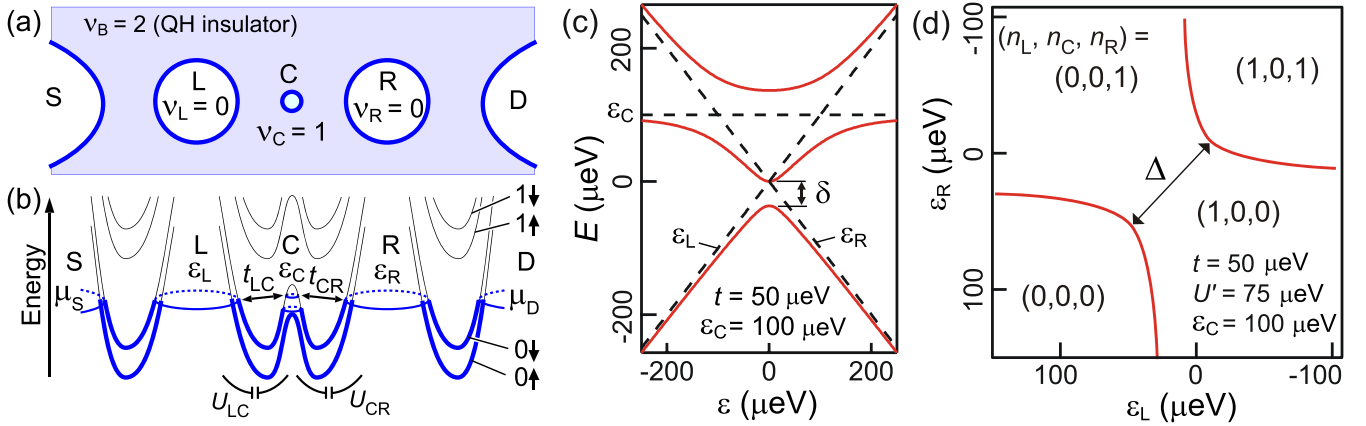


FIG. 1. (a) Schematic illustration of a triple QAD (L, C, and R) between the source (S) and drain (D) in a QH insulator at $\nu_B = 2$. Local filling factors $\nu_L = 0$, $\nu_C = 1$, and $\nu_R = 0$ are assumed. (b) Energy diagram of spin-resolved Landau levels ($0\uparrow$, $0\downarrow$, $1\uparrow$, and $1\downarrow$) for the triple QAD. Bound states with energies ε_L , ε_C , and ε_R are coupled with tunnel coupling t_{LC} and t_{CR} , and electrostatic coupling U_{LC} and U_{CR} . (c) Eigenenergies of a one-electron triple QAD with $t = 50 \mu\text{eV}$ (the solid lines) and $t = 0$ (the dashed lines) as a function of $\varepsilon \equiv \varepsilon_L - \varepsilon_R$. (d) Stability diagram of charge states (n_L, n_C, n_R) for the triple QAD with $t = 50 \mu\text{eV}$, $U' = 75 \mu\text{eV}$, and $\varepsilon_C = 100 \mu\text{eV}$.

The hybridization of QADs L, C, and R can be described by the effective one-electron Hamiltonian

$$H_1 = \begin{pmatrix} \varepsilon_L & t_{LC} & 0 \\ t_{LC}^* & \varepsilon_C & t_{CR} \\ 0 & t_{CR}^* & \varepsilon_R \end{pmatrix} \quad (1)$$

for the first electron from the reference electron numbers in the system. Here, we consider only the nearest-neighbor tunneling t_{LC} and t_{CR} by neglecting distant tunneling between L and R. Only a single energy level in each QAD is considered for simplicity. Figure 1(c) shows the eigenenergies of the system as a function of the energy bias $\varepsilon \equiv \varepsilon_L - \varepsilon_R$ for $\varepsilon_L = \varepsilon/2$ and $\varepsilon_R = -\varepsilon/2$ at $\varepsilon_C = 100 \mu\text{eV}$ and $t_{LC} = t_{CR} = t = 50 \mu\text{eV}$ (the solid lines). As compared to the uncoupled case with $t_{LC} = t_{CR} = 0$ (the dashed lines), finite energy splitting δ is seen in the hybridized states (the solid lines) around the crossing of ε_L and ε_R . The bottom trace shows the ground-state energy $E_1^{(\text{GS})}$ of the one-electron system. The splitting $\delta = (\sqrt{\varepsilon_C^2 + 8t^2} - |\varepsilon_C|)/2$ at $\varepsilon_L = \varepsilon_R = 0$ is tunable with ε_C even when t is fixed. The second-order tunneling can be seen in the approximated form of $\delta \simeq 2t^2/|\varepsilon_C|$ for $|\varepsilon_C| \gg t$.

We study the higher-order tunneling by investigating the charging diagram of the triple QADs. The system accommodates (n_L, n_C, n_R) numbers of excess electrons in the respective QADs by varying ε_L and ε_R . In the absence of distant electrostatic coupling between L and R, the two-electron Hamiltonian reads

$$H_2 = \begin{pmatrix} \varepsilon_L + \varepsilon_C + U_{LC} & t_{CR} & 0 \\ t_{CR}^* & \varepsilon_L + \varepsilon_R & t_{LC} \\ 0 & t_{LC}^* & \varepsilon_R + \varepsilon_C + U_{CR} \end{pmatrix} \quad (2)$$

for the charge bases $(1,1,0)$, $(1,0,1)$, and $(0,1,1)$. The ground-state energy $E_2^{(\text{GS})}$ of the two-electron system can be obtained by diagonalizing H_2 . The system takes the charge state (n_L, n_C, n_R) with minimum energy, as shown in the stability diagram of Fig. 1(d) in the ε_L - ε_R plane. The boundaries among three regions with different total electron number $n =$

$n_L + n_C + n_R$ are shown by the red lines. Here, we investigate the minimum spacing Δ between the charge states $(0,0,0)$ and $(1,0,1)$ in this paper. For $t_{LC} = t_{CR} \equiv t$ and $U_{LC} = U_{CR} \equiv U'$, Δ is given by

$$\Delta = \frac{U' - |\varepsilon_C| + 2\sqrt{\varepsilon_C^2 + 8t^2} - \sqrt{(|\varepsilon_C| + U')^2 + 8t^2}}{2}, \quad (3)$$

which includes $\delta = \frac{1}{2}(\sqrt{\varepsilon_C^2 + 8t^2} - |\varepsilon_C|)$. The remainder $U'' \equiv \Delta - \delta$ can be understood as emergent electrostatic coupling induced by the second-order tunneling ($U'' \simeq 2t^2 \frac{U'}{|\varepsilon_C|(|\varepsilon_C| + U')}$ for $|\varepsilon_C| \gg t$). Therefore, observation of finite Δ induced at small $|\varepsilon_C|$ suggests tunable coupling of δ and U'' . Note that symmetric parameters ($t_{LC} = t_{CR}$ and $U_{LC} = U_{CR}$) are assumed for simplicity, and tunable coupling is expected even with asymmetric parameters.

The model is equivalent to that for triple QDs. While similar three-level systems can be seen in previous studies on QDs and atoms [21–23], their realization in QADs would provide a significant step for coherent control of quasiparticles.

III. EXPERIMENT

A. Sample and measurement setup

Our sample was fabricated in a standard AlGaAs/GaAs heterostructure with two-dimensional electron gas located at 100 nm below the surface. With an electron density of $\approx 2.75 \times 10^{15} \text{ m}^{-2}$, a QH state at $\nu_B = 2$ can be prepared by applying perpendicular magnetic field $B \simeq 5 \text{ T}$. Two airbridge gates with Ti (thickness of 30 nm) and Au (270 nm) layers were fabricated by using electron-beam lithography with a triple layer resist [24,25]. Each gate has a small pillar of diameter $D = 300 \text{ nm}$ and is connected to the lead electrode through the bridge of length $L = 3 \mu\text{m}$, width $W = 300 \text{ nm}$, and bridge height $h = 150 \text{ nm}$, as shown in Fig. 2(a). The two pillars are separated by distance $d = 500 \text{ nm}$. This device was originally designed to form two QADs around the pillars [the red circles in Fig. 2(a)]. Such airbridge gates

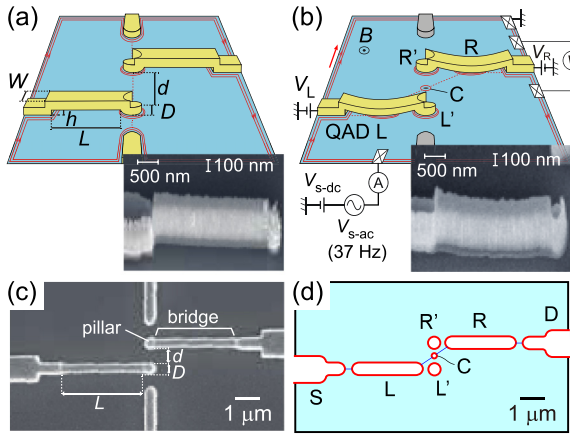


FIG. 2. (a) Schematic illustration of the original QAD design with two airbridge gates and two side gates. Two QADs are expected to form around the pillars. The inset shows the 45°-tilt SEM image of an undeformed bridge used in our previous experiments [24,25]. (b) Schematic illustration of the present sample with two deformed gates. Measurement setup for transport through QAD L and R under the deformed bridge and impurity-induced QAD C is shown. The inset shows the 45°-tilt SEM image of the deformed airbridge (shrunk horizontally to highlight the deformation). (c) A top view SEM image of the present sample with the deformed bridges (taken after the measurement). (d) Schematic geometry of QAD L, C, and R between the source (S) and drain (D) channels. The QAD L' and R' might be absorbed in L and R.

worked nicely in our previous study [24,25]. However, for the particular device used in this paper, it turned out that the airbridges have been deformed, as shown in Fig. 2(b) with an SEM picture taken after the measurement. The central part of the bridge is touching the surface of the heterostructure. We noticed later that the deformation was introduced during the post photo-lithography process with PMGI, which was not used for the previous devices. Note that the deformation of the bridge is reproducible with the same process, whereas the detailed mechanism of the deformation is not known.

As a result of the deformation, a relatively large QAD with the area of $LW \simeq 1 \text{ } (\mu\text{m})^2$ should be formed under the deformed bridge. This area is comparable to those of typical QADs seen in the literature [26]. We find that such QADs, referred to as QADs L and R, under the deformed bridges work nicely in this paper. However, we did not find any characteristics associated with the intended QADs L' and R' under the pillars (see Sec. III C).

We take advantage of localized states present in our device. While they are randomly distributed in the sample, we focus on a specific localized state, which acts as QAD C, located between QADs L and R. Following measurements suggests that QAD C with the area of 0.02–0.04 $(\mu\text{m})^2$, equivalent to a circle with a diameter of 160–230 nm, is located in the middle of QAD L and R, as illustrated in Fig. 2(b) (see Sec. III B). Figure 2(c) shows the top view SEM image of the present device taken after the measurements, where pillars (deformed), airbridges, and lead electrodes are seen. Schematic locations of QADs are illustrated in Fig. 2(d), while QADs L' and R' might be merged into L and R, respectively.

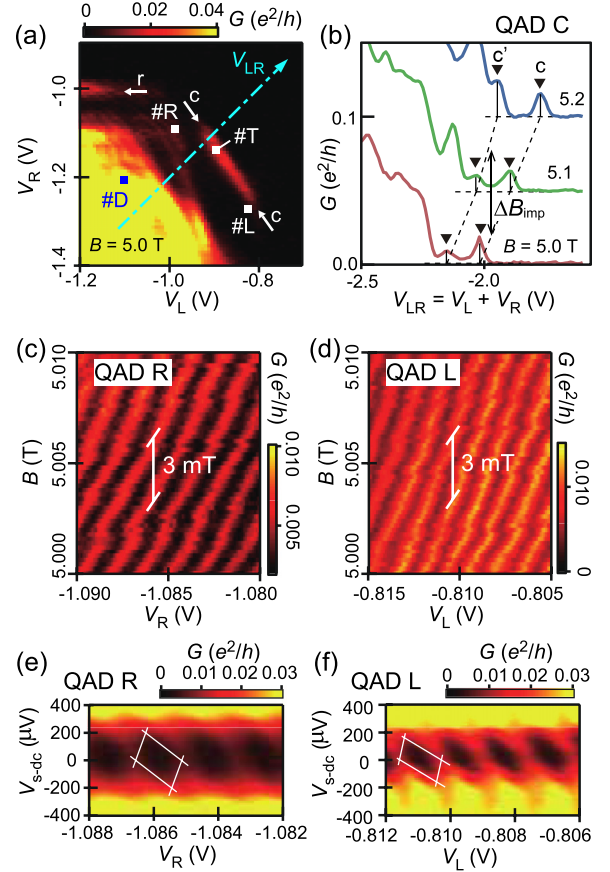


FIG. 3. (a) Color plot of differential conductance G as a function of V_L and V_R at $B = 5.0 \text{ T}$ and $V_{s-dc} = 0$. The peak between the arrows labeled c is the CB peak associated with QAD C. Single QADs L and R are investigated at conditions marked by #L and #R, respectively. Double and triple QADs are investigated at conditions marked by #D and #T, respectively. (b) G as a function of $V_{LR} = V_L + V_R$ along the dot-dashed line in (a) at different magnetic fields. Each trace is offset by $0.05e^2/h$ for clarity. (c), (d) G as a function of B and each gate voltage. (e), (f) Coulomb diamond characteristics seen in G as a function of bias voltage V_{s-dc} and the gate voltage, V_R for QAD R in (e) and V_L for QAD L in (f). The white parallelogram shows an approximate CB region.

The transport through the QADs is investigated by applying ac voltage $V_{s-ac} = 30 \text{ } \mu\text{V}$ at 37 Hz and dc voltage V_{s-dc} ($= 0$ unless otherwise noted) to the source and measuring the ac voltage drop V between the voltage probes with a lock-in amplifier [Fig. 2(b)]. The differential conductance G is estimated from the relation $G = (2e^2/h) \times (V/V_{s-ac})$. All measurements were performed in a dilution refrigerator with a base temperature of about 100 mK.

B. Localized state as QAD C

Figure 3(a) shows a color plot of conductance G over the wide ranges of V_L and V_R at $B = 5.0 \text{ T}$. Whereas the Coulomb oscillations of QAD L and R are not visible with this coarse scan, several current peaks associated with localized states are resolved. For example, the horizontal line at $V_R \simeq -1.0 \text{ V}$ (marked by the arrow labeled r) should be associated with a localized state near the right gate with V_R but far from the

left gate with V_L . We focus on a specific localized state that exhibits the current peak marked by the arrows labeled *c*. As this peak is elongated in the lower-right direction with a slope of $dV_R/dV_L = -1.45$ in the figure, the state is almost equally coupled to the two gates, and thus should be located at around the center of the two gates (slightly closer to the left gate). We shall use this localized state as QAD C in the following.

Figure 3(b) shows the conductance traces taken by simultaneously changing V_L and V_R along the dot-dashed line labeled V_{LR} in Fig. 3(a) for several B values. In Fig. 3(b), the two peaks labeled *c* and *c'* evolve in a similar manner with B , as shown by the dashed lines, implying that they are two consecutive CB peaks for the same impurity. The corresponding magnetic field period of about $\Delta B_{\text{imp}} = 0.1\text{--}0.2$ T suggests that the area enclosed by the bound state is $S_{\text{imp}} = (h/e)/\Delta B_{\text{imp}} \simeq 0.02\text{--}0.04$ (μm)² by assuming local filling factor $\nu_C = 1$. If the bound state is circular, its diameter of 160–230 nm can fit in between the two gates with the distance of $d = 500$ nm, as illustrated in Fig. 2(d).

In Sec. II E, we focus on peak *c* of Fig. 3(b), where rich characteristics associated with QADs L, C, and R show up in the fine sweep of V_R and V_L .

C. Single QAD L and R

The QADs L and R were investigated separately by focusing on the conditions #L and #R, respectively, in the V_R - V_L plane of Fig. 3(a). The transport is effectively determined by each QAD under the asymmetric gate voltages, where other QADs are strongly coupled to the leads. CB oscillations of QAD R can be seen in fine sweeps of V_R and B , as shown in Fig. 3(c). Its oscillation period in B is $\Delta B_R \simeq 3$ mT, which corresponds to the area enclosed by the bound states, $S_R = \frac{1}{2} \frac{h}{e} \frac{1}{\Delta B_R} \simeq 0.7$ (μm)². Here, the factor $\frac{1}{2}$ is used for the two occupied spin-resolved Landau levels with $\nu_B - \nu_R = 2$, where bound states associated with the two Landau levels strongly interacted electrostatically [4–7]. This S_R is comparable to the area of the deformed bridge [$LW = 1.0$ (μm)²] but far from the area of the pillar [≈ 0.07 (μm)²] in consistency with QAD R being formed under the deformed gate.

The Coulomb diamond characteristics of QAD R are obtained by applying $V_{s\text{-dc}}$ and V_R , as shown in Fig. 3(e). The CB region with $G \approx 0$ is seen in the voltage range $|V_{s\text{-dc}}| \lesssim 200$ μV , as illustrated by a white parallelogram as a guide. This measures the addition energy $U_R \simeq 200$ μeV , which includes the on-site Coulomb charging energy and level spacing of the bound states. This value is comparable to typical values of reported QADs with similar sizes [26]. The energy of each bound state can be shifted by $\alpha_R \Delta V_R$ with small change ΔV_R in V_R , where the lever arm factor $\alpha_R \simeq -0.13e$ is roughly estimated from the size of the parallelogram.

Similarly, QAD L investigated at around condition #L shows CB oscillations in Fig. 3(d). The oscillation period $\Delta B_L \simeq 3$ mT also suggests that the QAD is formed under the deformed bridge. The two QADs show similar oscillation periods in B as well as their gate voltages (V_R and V_L). The Coulomb diamond characteristics for QAD L in Fig. 3(f) show smaller blockade regions with somewhat smaller addi-

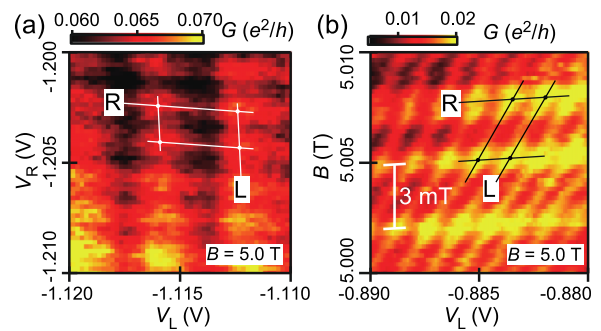


FIG. 4. (a) Color plot of conductance G as a function of V_L and V_R at around condition #D in Fig. 3(a) for uncoupled QADs L and R showing parallelogram patterns (the white lines). (b) G as a function of V_L and B at $V_R = -1.135$ V, showing another example of uncoupled QADs L and R. The black lines labeled L and R represent CB peaks attributed to QAD L and R, respectively.

tion energy $U_L \simeq 180$ μeV and $\alpha_L \simeq -0.15e$. Similar QADs with small differences are well reproduced by the deformed bridges.

D. Uncoupled double QAD

Transport through QADs L and R with a negligible role of QAD C can be seen when large negative voltages, V_L and V_R , are applied. Figure 4(a) shows such Coulomb oscillations in the fine sweep of V_L and V_R at around condition #D in Fig. 3(a). The oscillations for QAD L (the vertical lines) and R (the horizontal lines) are resolved but not influenced by each other with no measurable splitting at their crossings, as shown by the white parallelogram in Fig. 4(a). This is the signature of negligible tunnel and electrostatic couplings, as studied with conventional QDs [15].

Another example of uncoupled QADs is shown in the B - V_L plane of Fig. 4(b), where the parallelogram pattern (the black lines) for CB oscillations of QAD L and R is resolved. Whereas this V_L and V_R range is the condition where triple QAD formation is expected [#T in Fig. 3(a)], a negligible role of QAD C is seen probably due to small tunneling (t_{LC} , t_{RC}) in this B range. The magnetic field periods, $\Delta B_R \simeq 3$ mT and $\Delta B_L \simeq 3$ mT, are similar to those obtained for single QADs. Therefore, QADs L and R are stably formed in the wide range of V_L and V_R .

The above data show that distant QADs L and R are uncoupled with negligible tunneling ($t_{LR} \simeq 0$) and electrostatic ($U_{LR} \simeq 0$) couplings. However, the two QADs can be coupled by introducing QAD C, as shown in the next subsection.

E. Triple QAD

Coupling of QADs L, C, and R can be found in Fig. 5, where G was measured with a fine sweep of V_L and V_R at various magnetic fields. The sweep ranges of V_L and V_R are adjusted for each B to keep the focus on the resonance with QAD C [the equivalent condition is marked by #T in Fig. 3(a)]. Fine oscillations are superimposed on the broad peak of QAD C. Rich characteristics ranging from parallelogram to honeycomb patterns are seen. In addition, sharp diagonal lines (some marked by the arrows) show up in the limited range of

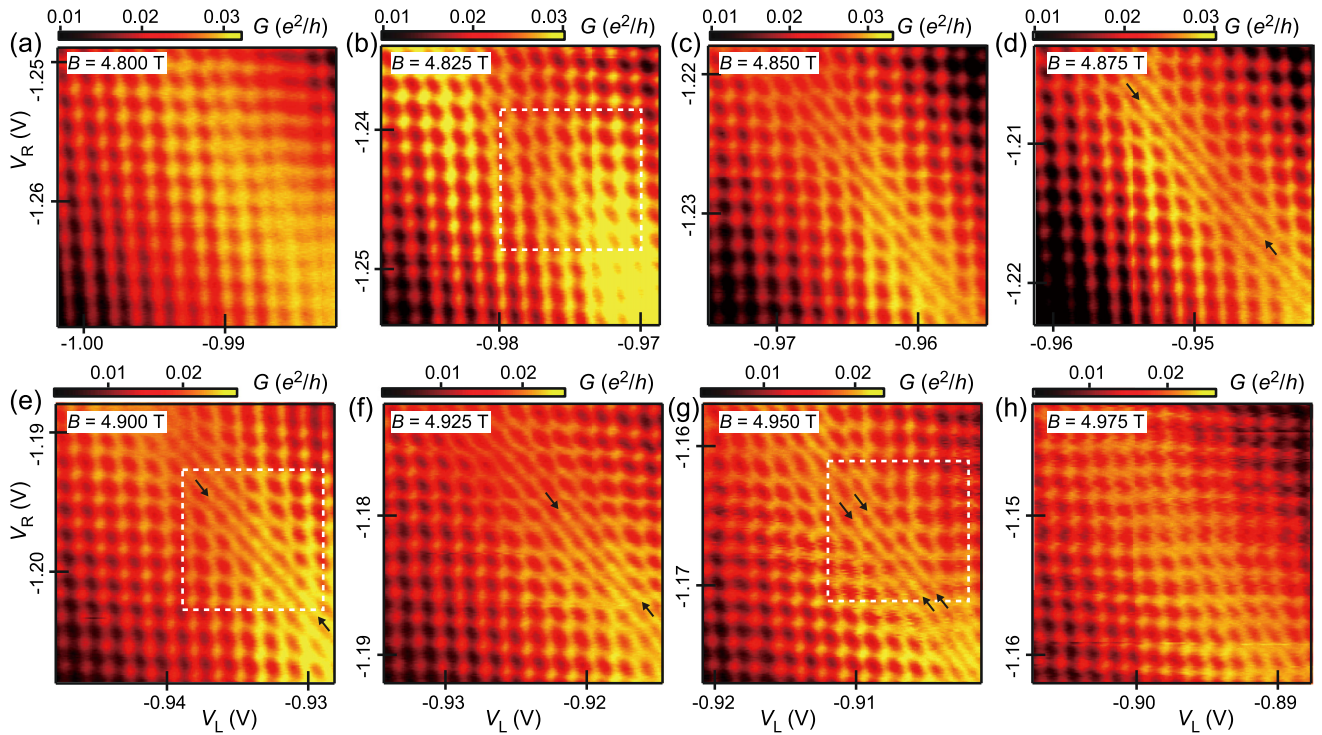


FIG. 5. (a)–(h) Color plots of G as a function of V_L and V_R at different magnetic fields from 4.800 T in (a) to 4.975 T in (h). For each B , the sweep ranges of V_L and V_R are adjusted to focus on the broad CB peak of the impurity QAD C. Some diagonal straight lines are highlighted by the arrows.

$4.875 \leq B \leq 4.950$ T. Some representative characteristics are analyzed in the following.

First, we focus on the white dashed region of Fig. 5(e) at $B = 4.900$ T, which is enlarged in Fig. 6(a). Strikingly, one of the CB peaks follows the single straight diagonal line

between the two arrows labeled ξ . This line is located around the center of the CB peak of QAD C, and the linewidth is much sharper than the peak width of QAD C. The meaning of the diagonal line is clarified by analyzing the Coulomb oscillations of QADs L and R. The CB peaks of QAD L

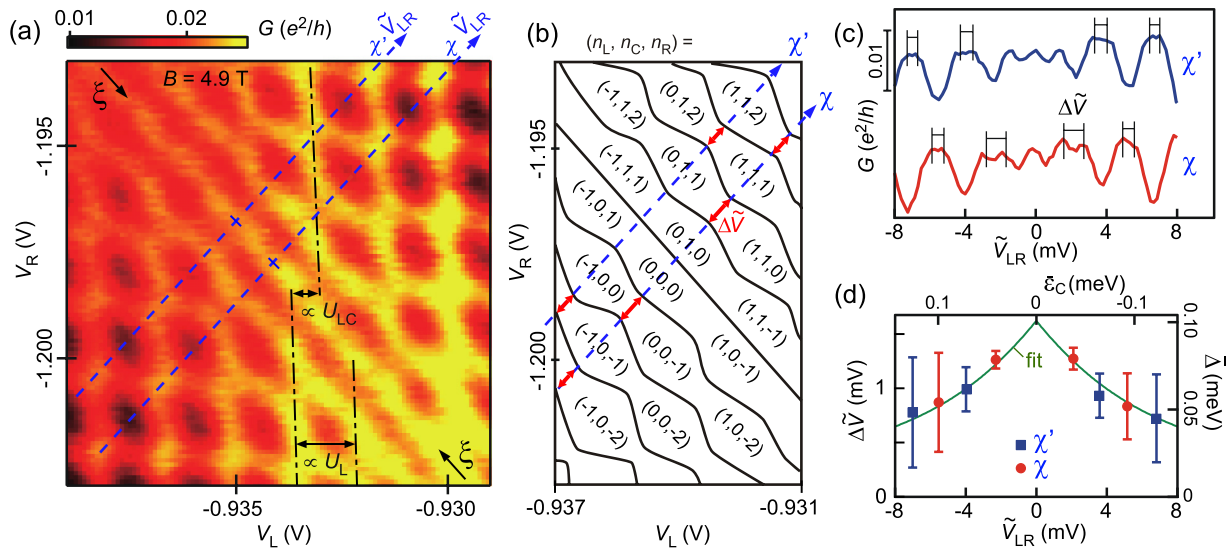


FIG. 6. (a) G as a function of V_L and V_R measured at 4.900 T [equivalent gate-voltage condition is marked by #T in Fig. 3(a)]. The straight diagonal line is indicated by two arrows labeled ξ . Other honeycomb and parallelogram patterns are almost symmetric about the diagonal line. The spacings of CB oscillations (the dot-dashed lines) for QAD L reflect U_L and U_{LC} . (b) Schematic charge stability diagram with excess electron numbers (n_L, n_C, n_R) for (a). The red arrows indicate the spacing $\Delta\tilde{V}$ of the anticrossings. (c) Cross-sectional slices of G along the lines χ and χ' as a function of relative gate voltage \tilde{V}_{LR} in $V_{LR} = V_L + V_R$ measured from the straight diagonal line in (a). The anticrossing is represented by the vertical lines as guides to the eye. (d) The anticrossing $\Delta\tilde{V}$ in V_{LR} is plotted as a function of \tilde{V}_{LR} for the slices χ and χ' in (c). The right axis $\bar{\Delta} = |\frac{1}{2}\alpha_{\Delta}\Delta\tilde{V}|$ is converted with $\alpha_{\Delta} = -0.13e$. The top axis $\bar{\epsilon}_C$ is estimated from the fit (the green line) with the model.

[the dot-dashed lines in Fig. 6(a)] are abruptly shifted across the diagonal line. This shift suggests that the charge state of QAD C is changed from $n_C = 0$ (the lower-left side) to 1 (the upper-right side), which influences the potential of QAD L. Therefore, we define $\varepsilon_C = 0$ on the diagonal line. The shift measures the electrostatic coupling $U_{LC} \simeq 75 \mu\text{eV}$ between QAD L and C. Similar shift is seen for CB peaks of QAD R (not marked), from which $U_{CR} \simeq 75 \mu\text{eV}$ is estimated. It should be noted that the straight diagonal line is associated with a special resonance of hybridized states under symmetric conditions of the triple QAD, as elaborated in Sec. IV.

The current profile in the vicinity of the diagonal line shows a clear rounded honeycomb pattern, which manifests finite coupling between QAD L and R. The honeycomb pattern gradually changes to the parallelogram pattern toward the upper-right and lower-left corners. The corresponding charge stability diagram is sketched in Fig. 6(b), where each region is labeled with excess electron numbers (n_L, n_C, n_R) from a reference. We investigate the minimum spacing $\Delta\tilde{V}$ between the rounded charge boundaries, which corresponds to Δ in Eq. (3). The overall conductance profile is mirror symmetric about the diagonal line and periodic along the diagonal line (the upper-left direction). This feature suggests that the spacing $\Delta\tilde{V}$ is dominantly changed only by $|\varepsilon_C|$, i.e., the distance from the diagonal line. Other parameters, specifically t_{LC} and t_{CR} , are unchanged within the sweep range of V_L and V_R . Otherwise, the conductance pattern should change in a nonsymmetric way. These characteristics support the demonstration of tunable coupling with cotunneling.

Cross-sectional current profiles passing through several anticrossing conditions are shown in Fig. 6(c). Here, two cross sections χ and χ' pick up different anticrossings as illustrated by the dashed lines in Figs. 6(a) and 6(b). The axis \tilde{V}_{LR} denotes the relative gate voltage in $V_{LR} = V_L + V_R$ measured from the central diagonal line ($\varepsilon_C = 0$). The splitting $\Delta\tilde{V}$ is shown by the bars in Fig. 6(c). The precise values and their errors are determined from the overall pattern in Fig. 6(a). For example, the peak (spot) slightly elongated to the upper-right direction suggests finite splitting, even if the two split peaks are unresolved in the cross-sectional plot. The estimated $\Delta\tilde{V}$ is plotted as a function of \tilde{V}_{LR} in Fig. 6(d), in which the symmetric variation of $\Delta\tilde{V}$ is seen.

$\Delta\tilde{V}$ can be converted into the splitting energy, $\bar{\Delta} = |\frac{1}{2}\alpha_\Delta\Delta\tilde{V}|$, by using the lever arm factor $\alpha_\Delta = -0.13e$ (see Appendix A), as shown in the right scale. To see the consistency with the proposed scheme, we assume equal tunnel coupling ($t_{LC} = t_{CR} = t$), which will be justified in Sec. IV A, and linear dependence of $\bar{\varepsilon}_C = \eta\tilde{V}_{LR}$ on \tilde{V}_{LR} with unknown factor η . Here, symbols with a bar ($\bar{\Delta}$ and $\bar{\varepsilon}_C$) denote the quantities obtained for different charge states, while the original Δ and ε_C are defined for a given charge state. We apply Eq. (3) by replacing Δ and ε_C with $\bar{\Delta}$ and $\bar{\varepsilon}_C$ for the fitting to the data. By using $U' = U_{LC} = U_{CR} = 75 \mu\text{eV}$, the measured $\bar{\Delta}$ is well reproduced by the fitting [the solid green line in Fig. 6(d)] with adjusted parameters, $t = 50 \mu\text{eV}$ and $\eta = -0.02e$. Here, tuning of $\bar{\varepsilon}_C$ is induced by the purely capacitive effect with $\varepsilon_C = \eta'\tilde{V}$ but partially compensated by the excess charge of the QADs (n_L and n_R). They are related by $\bar{\varepsilon}_C = \eta'\tilde{V} + U_{LC}n_L + U_{CR}n_R$, where $n_L = n_R = 0$ is defined for the region at $\varepsilon_C = 0$ [see Fig. 6(b)]. We obtained

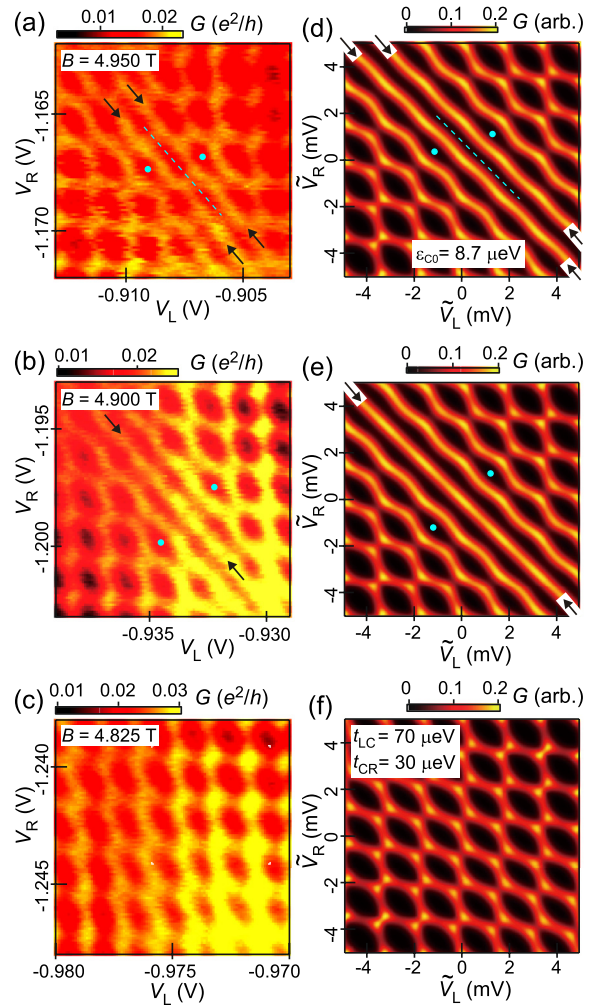


FIG. 7. (a)–(c) Measured G as a function of V_L and V_R at $B = 4.950$ T in (a), 4.900 T in (b), and 4.825 T in (c). Straight diagonal lines are marked by the arrows in (a) and (b), but not seen in (c). (d)–(f) Calculated G as a function of \tilde{V}_L and \tilde{V}_R . The offset energy for ε_C is $\varepsilon_{C0} = 8.7 \mu\text{eV}$ in (d) and $\varepsilon_{C0} = 0$ in (e) and (f). The tunnel couplings are $t_{LC} = t_{CR} = 50 \mu\text{eV}$ in (d) and (e), and $t_{LC} = 70 \mu\text{eV}$ and $t_{CR} = 30 \mu\text{eV}$ in (f). $U_L = U_R = 200 \mu\text{eV}$ and $U_{LC} = U_{CR} = 75 \mu\text{eV}$ were used for the calculation.

$\eta' = -0.06e$ from the relations. This η' does not contradict the realistic lever arm factors in our sample (see Appendix A), and supports our scheme. Therefore, the result indicates that the total coupling energy Δ as well as the tunnel coupling δ are successfully controlled with the energy of the localized state in the range of $0 < \delta < \sqrt{2}t$ ($\simeq 70 \mu\text{eV}$ in the present case).

The tunable tunnel coupling can be confirmed in the wide range of B , as shown in Fig. 5. In all cases, one can see honeycomb patterns near the center of the CB peak of QAD C and parallelogram patterns near the upper-right and lower-left corners. However, the precise patterns including the diagonal lines near the CB peak of QAD C change significantly with B . The white dashed regions in Figs. 5(b), 5(e), and 5(g) are magnified in Figs. 7(b), 7(c), and 7(a), respectively. Two diagonal lines (indicated by the arrows) are resolved at $B = 4.95$ T in Fig. 7(a), whereas only a single line is seen at $B = 4.90$ T in Fig. 7(b) [the same data as Fig. 6(a)]. No clear

diagonal line is resolved at $B = 4.825$ T in Fig. 7(c) [see also $B = 4.800$ and 4.975 T in Figs. 5(a) and 5(h), respectively], while the honeycomb pattern with finite splitting is seen. Full understanding requires detailed analysis on the symmetry of the QAD parameters, as shown in the next section.

IV. SYMMETRY OF TRIPLE QAD

A. System Hamiltonian

First of all, we should note the differences in electronic states between QADs and standard QDs. For QDs at zero or low magnetic fields, the energy levels are strongly influenced by many-body effects with direct and exchange interactions as well as single-particle orbitals and Zeeman splittings. As a result, CB oscillations are generally aperiodic and thus charge stability diagrams of multiple QDs are complicated with many jumps in the CB conditions [21–23,27–33]. In contrast, the energy quantization of QADs in the integer QH system is dominated by the Aharonov-Bohm effect, which determines the area of the bound state under uniform B . Therefore, the energy spacing is almost constant for a smooth QAD potential for each spin-resolved Landau level. When multiple Landau levels are involved for each QAD, occupation of the inner Landau level is well screened by the outer one. Therefore, CB oscillations are periodic with a constant addition energy U for different charge states [34]. The deviation from the periodic pattern is studied with the hybridization of the system, as shown below.

In this paper, a symmetric QAD with $t_{LC} = t_{CR}$ and $U_{LC} = U_{CR}$ is assumed for proposing the tunable second-order coupling scheme. While the symmetry is not required just for tuning the tunnel coupling, we should investigate the role of the symmetry in the hybridization. Interestingly, we found that the diagonal straight line observed in Fig. 6(a) is the signature of the symmetry.

Generally, CB peaks appear when the ground-state energy $E_n^{(GS)}$ of the n -electron system coincides with that $E_{n+1}^{(GS)}$ of the $(n+1)$ -electron system, where the electrochemical potential $\mu = E_{n+1}^{(GS)} - E_n^{(GS)}$ of the system equals the chemical potentials (defined to be zero) of the leads. The appearance of the diagonal straight line suggests that this equality ($E_n^{(GS)} = E_{n+1}^{(GS)}$) is satisfied on the diagonal line over several charge states. In the presence of significant nearest-neighbor tunneling ($t_{LC}, t_{CR} \neq 0$), the most probable situation is that the n - and $(n+1)$ -electron systems share the identical eigenenergies including the ground-state one with the same form of Hamiltonians H_n and H_{n+1} .

To see this happens, the excess charges (n_L, n_C, n_R) that belong to the n - and $(n+1)$ -electron systems are listed in Fig. 8(a) with an integer m in such a way that electrons are moved from the left to the right by tunneling processes with t_{LC} and t_{CR} under the constraint $n_C \in \{0, 1\}$. The total energy of state $\mathbf{n} = (n_L, n_C, n_R)$ in the absence of tunneling can be written as

$$E_{\mathbf{n}} = \sum_{i=L,C,R} \left[n_i \varepsilon_i + \frac{1}{2} n_i (n_i - 1) U_i \right] + n_L n_C U_{LC} + n_C n_R U_{CR}. \quad (4)$$

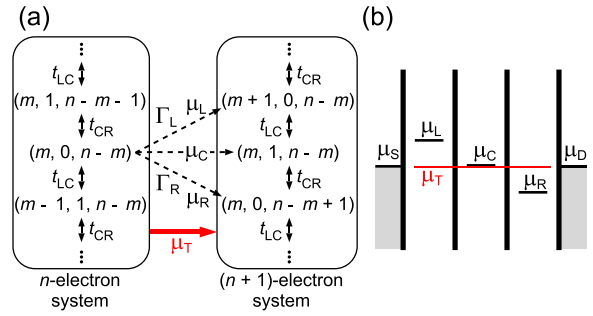


FIG. 8. (a) Tunnel coupling (t_{LC} and t_{CR}) between charge states (n_L, n_C, n_R) in n - and $(n+1)$ -electron systems. (b) Chemical potential diagram for the triple QAD. Sequential tunneling between the unhybridized states can be characterized by the simple electrochemical potentials μ_L, μ_C , and μ_R . Correct electrochemical potential μ_T should be considered for the hybridized triple QAD.

Therefore, the matrix form of the Hamiltonian with charge bases has diagonal elements of E_n and nearest-neighbor off-diagonal elements t_{LC} and t_{CR} . H_1 and H_2 in Eqs. (1) and (2) are examples of $n = 1$ and $m = 1$ in the reduced Hilbert space (only for three charge states). The conditions for identical Hamiltonians ($H_n = H_{n+1}$) are $t_{LC} = t_{CR}$, $U_{LC} = U_{CR}$ ($\equiv U'$), $U_L = U_R$ ($\equiv U$), $\varepsilon_C = -nU'$, and $\varepsilon_L + \varepsilon_R = -nU$. The straight diagonal line is expected to appear if all conditions are met.

The last two conditions can be written with convenient but misleading electrochemical potentials $\mu_L = \varepsilon_L + mU$, $\mu_C = 0$, and $\mu_R = \varepsilon_R + (n-m)U$ for adding an electron to QADs L, C, and R, respectively, from charge state $(m, 0, n-m)$ [the dashed arrows in Fig. 8(a)], where the hybridization is not considered at all. Notice $\mu_L + \mu_R = 0$ under the required conditions, as shown in the energy diagram of Fig. 8(b). Conventional sequential-tunneling transport is not allowed for this condition ($\mu_L \neq \mu_C \neq \mu_R$), and thus does not explain the appearance of the diagonal line. In the presence of significant $t_{LC} = t_{CR}$, the charge states of n - and $(n+1)$ -electron systems are strongly hybridized with the identical matrix form of Hamiltonians, and thus the correct electrochemical potential of the triple QAD is $\mu_T = 0$ on the diagonal line. Therefore, the hybridization plays an essential role in the appearance of the diagonal line.

The appearance of the diagonal line implies that the system satisfies all conditions. As our sample shows $U_{LC} \simeq U_{CR}$ and $U_L \simeq U_R$, $t_{LC} = t_{CR}$ and $\mu_C = 0$ must be satisfied within the experimental allowance. Considering the variations of the patterns at different B 's in Fig. 5, the data in Fig. 6(a) could be the special case close to the symmetric conditions.

B. Numerical simulation

The current profiles under the symmetric and nonsymmetric conditions are calculated by using the standard master equation [35]. The two gate voltages, \tilde{V}_L and \tilde{V}_R , control the electrostatic potentials of the three QADs, $\varepsilon_L, \varepsilon_C$, and ε_R , with the lever arm factors, $\alpha_R = \alpha_L = -0.13e$, $\alpha_{CL} = \alpha_{CR} = -0.06e$, and $\alpha_{LR} = \alpha_{RL} = 0$, and offset energies $\varepsilon_{L0} = \varepsilon_{R0} = 0$ and ε_{C0} (see Appendix A for their definitions). The Hamiltonian H_n is diagonalized to obtain the eigenstates. The current through the triple QAD is calculated for small bias voltage

$V_S = 30 \mu\text{eV}$ between the source and the drain at electron temperature T ($k_B T = 10 \mu\text{eV}$). Tunneling rates to the source and the drain are fixed at $\Gamma_S = \Gamma_D = 1 \text{ GHz}$. The calculation scheme for the wide range of charge states is described in Appendix B.

Figure 7(e) shows the calculated G under the symmetric condition with $t_{LC} = t_{CR} = 50 \mu\text{eV}$, $U_L = U_R = 200 \mu\text{eV}$, $U_{LC} = U_{CR} = 75 \mu\text{eV}$, and $\varepsilon_{C0} = 0$, where identical Hamiltonian $H_n = H_{n+1}$ is expected at $\tilde{V}_L + \tilde{V}_R = 0$. The central diagonal line (marked by the arrows) is reproduced at $\tilde{V}_L + \tilde{V}_R = 0$. The honeycomb pattern is clearly resolved near the line, and the splitting is gradually decreasing toward the upper-right and lower-left corners. All features are symmetric about the diagonal line (highlighted by the dot pair). They are qualitatively the same as the experimental features including the mirror symmetry in Fig. 7(b), which suggests that the symmetric conditions are satisfied in the experiment.

When a small energy offset of $\varepsilon_{C0} = 8.7 \mu\text{eV}$ is introduced to the conditions for Fig. 7(e), the pattern is no longer mirror symmetric about the diagonal line, as shown in Fig. 7(d). The pattern shows the glide reflection symmetry (highlighted by the dot pair) about the dashed line between the double diagonal line (marked by the arrows). Such glide reflection symmetry is seen in our experimental data of Fig. 7(a).

Identical tunneling with $t_{LC} = t_{CR}$ is the essential condition. Our simulation (not shown) suggests that we would not recognize the deviation from the straight diagonal line if the asymmetry is not large ($\gamma \equiv \left| \frac{t_{LC} - t_{CR}}{t_{LC} + t_{CR}} \right| \lesssim 0.1$). When large $\gamma = 0.4$ ($t_{LC} = 70 \mu\text{eV}$ and $t_{CR} = 30 \mu\text{eV}$) is assumed in the simulation, the diagonal line disappears as shown in Fig. 7(f). While the honeycomb pattern is seen in the entire region of the figure, the splitting shows gentle variation. A similar pattern is seen in our data of Fig. 7(c), whereas the parameters for Fig. 7(f) were not adjusted to the experimental data.

Identical Coulomb interactions with $U_{LC} = U_{CR}$ and $U_L = U_R$ are important for the periodicity along the diagonal line. Some diagonal lines are visible only for a few oscillation periods, which may be related to small asymmetry in the Coulomb interactions.

Whereas we observed smooth tuning of honeycomb patterns with gate voltages, we do not see systematic variation with the magnetic field. Slight change in magnetic field can induce drastic change in the stability diagram, which might be related to uncontrollable charging of localized states.

V. SUMMARY

We have proposed and demonstrated the triple QAD scheme for tunable coupling between two separate QADs by using cotunneling through the central QAD. The charge stability diagram of the system changes from the parallelogram pattern for the uncoupled case to the round honeycomb pattern for the coupled case by tuning the energy level of the central QAD. In a special case, the charge diagram shows diagonal straight lines as a signature of symmetric parameters of the triple QAD. Systematic variation of transport characteristics is studied by numerical calculation based on the master equation and by experiment with unintentional QADs and a localized state. The system can be made more tunable, if the localized state is replaced by an intentional QAD with an

independent gate. Our research has paved the way for further studies on multiple QADs in the integer and fractional QH states, such as a QAD array for anyon operations [14].

ACKNOWLEDGMENTS

This work was supported by JSPS KAKENHI Grants No. JP19H05603 and No. JP19K14630, and partially conducted at Nanofab in the Tokyo Institute of Technology supported by ‘‘Advanced Research Infrastructure for Materials and Nanotechnology (ARIM)’’ in Japan and at Materials Analysis Division, Open Facility Center in Tokyo Institute of Technology.

APPENDIX A: LEVER ARM FACTORS

The electrostatic potentials ε_L , ε_C , and ε_R can be changed by the gate voltages V_L and V_R with linear relations:

$$\begin{aligned}\varepsilon_L &= \alpha_L V_L + \alpha_{LR} V_R + \varepsilon_{L0}, \\ \varepsilon_C &= \alpha_{CL} V_L + \alpha_{CR} V_R + \varepsilon_{C0}, \\ \varepsilon_R &= \alpha_R V_R + \alpha_{RL} V_L + \varepsilon_{R0},\end{aligned}\tag{A1}$$

with lever arm factors (α 's) and offsets (ε_{L0} and so on). We estimated $\alpha_R \simeq -0.13e$ from the data in Fig. 3(e) and $\alpha_L \simeq -0.15e$ from Fig. 3(f). The CB oscillation periods of QAD L and R in Fig. 6(a) at #T are similar and close to the period of QAD R at #R. Therefore, the lever arm factor $\alpha_\Delta = -0.13e$ was used to obtain $\tilde{\Delta} = \frac{1}{2}\alpha_\Delta \Delta\tilde{V}$ in Fig. 6(d). The small ratios $\alpha_{LR}/\alpha_L \simeq \alpha_{RL}/\alpha_R \simeq 0.04$ are estimated from the slope of the CB oscillations (the dot-dashed lines for α_{LR}/α_L) in Fig. 6(a), but α_{LR} and α_{RL} are neglected in the numerical calculations for simplicity.

Unfortunately, we have no direct estimates on α_{CL} and α_{CR} . For example, α_{CL} describing the effect of the left gate on the QAD C potential should arise from the direct capacitive coupling and indirect coupling through QAD L. Whereas the former contribution is unknown, the latter can be estimated from $\alpha_L \frac{U_{LC}}{U_L} \simeq -0.05e$. As α_{CL} should be smaller than α_L , α_{CL} as well as α_{CR} should be in the range of $-0.05e \approx -0.13e$. If available, these values provide $\eta' \simeq \frac{1}{2}(\alpha_{CL} + \alpha_{CR})$ for the determination ε_C in Fig. 6(d). This parameter range does not contradict $\eta' = -0.06e$ obtained from the fitting to the data in Fig. 6(d). Therefore, we used $\alpha_{CL} = \alpha_{CR} = -0.06e$ in the numerical simulations.

APPENDIX B: CALCULATION OF TRIPLE-QAD CURRENT

We calculated the current through the triple QAD based on the master equation [35]. The electrochemical potential ε_i for the first excess electron only in QAD i can be controlled with excess gate voltages \tilde{V}_L and \tilde{V}_R , in the form of Eq. (A1). Here, ε_{C0} plays an important role in the stability diagram, and we set $\varepsilon_{L0} = \varepsilon_{R0} = 0$ and $\alpha_{LR} = \alpha_{RL} = 0$ for simplicity. The Hamiltonian H_n shown in Sec. IV A is diagonalized to obtain k th eigenenergy $E_{n,k}$ of the n -electron system. Transport through the triple QAD can be calculated by considering tunnel transitions to the leads. We assumed energy-independent tunneling rates Γ_S between the source and QAD L and Γ_D between QAD R and the drain. A master equation for occupation

probabilities of the eigenstates is constructed under a small bias voltage $V_S = 30 \mu\text{V}$ and thermal energy $k_B T = 10 \mu\text{V}$ in the leads. For each \tilde{V}_L and \tilde{V}_R , a few eigenstates with energies in the range of $E_{n,k} \leq E^{(\min)} + eV_S + 3k_B T$ contribute to the

transport, where $E^{(\min)}$ is the total ground-state energy for all possible n and k . The eigenstates within this energy range are considered in solving the master equation. The current was calculated from the steady-state occupation probabilities.

-
- [1] I. Sivan, H. K. Choi, J. Park, A. Rosenblatt, Y. Gefen, D. Mahalu, and V. Umansky, *Nat. Commun.* **7**, 12184 (2016).
- [2] M. P. Rössli, L. Brem, B. Kratochwil, G. Nicolí, B. A. Braem, S. Hennel, P. Märki, M. Berl, C. Reichl, W. Wegscheider *et al.*, *Phys. Rev. B* **101**, 125302 (2020).
- [3] M. P. Rössli, M. Hug, G. Nicolí, P. Märki, C. Reichl, B. Rosenow, W. Wegscheider, K. Ensslin, and T. Ihn, *Sci. Adv.* **7**, eabf5547 (2021).
- [4] S. W. Hwang, J. A. Simmons, D. C. Tsui, and M. Shayegan, *Phys. Rev. B* **44**, 13497 (1991).
- [5] C. J. B. Ford, P. J. Simpson, I. Zailer, D. R. Mace, M. Yosefin, M. Pepper, D. A. Ritchie, J. E. F. Frost, M. P. Grimshaw, and G. A. C. Jones, *Phys. Rev. B* **49**, 17456 (1994).
- [6] M. Kataoka, C. J. B. Ford, G. Faini, D. Mailly, M. Y. Simmons, D. R. Mace, C.-T. Liang, and D. A. Ritchie, *Phys. Rev. Lett.* **83**, 160 (1999).
- [7] H.-S. Sim, M. Kataoka, and C. Ford, *Phys. Rep.* **456**, 127 (2008).
- [8] S. M. Mills, A. Gura, K. Watanabe, T. Taniguchi, M. Dawber, D. V. Averin, and X. Du, *Phys. Rev. B* **100**, 245130 (2019).
- [9] S. M. Mills, D. V. Averin, and X. Du, *Phys. Rev. Lett.* **125**, 227701 (2020).
- [10] B. I. Halperin, A. Stern, I. Neder, and B. Rosenow, *Phys. Rev. B* **83**, 155440 (2011).
- [11] B. Rosenow and A. Stern, *Phys. Rev. Lett.* **124**, 106805 (2020).
- [12] J. Nakamura, S. Fallahi, H. Sahasrabudhe, R. Rahman, S. Liang, G. C. Gardner, and M. J. Manfra, *Nat. Phys.* **15**, 563 (2019).
- [13] J. Nakamura, S. Liang, G. C. Gardner, and M. J. Manfra, *Nat. Phys.* **16**, 931 (2020).
- [14] D. V. Averin and J. A. Nesteroff, *Physica E* **40**, 58 (2007).
- [15] W. G. van der Wiel, S. De Franceschi, J. M. Elzerman, T. Fujisawa, S. Tarucha, and L. P. Kouwenhoven, *Rev. Mod. Phys.* **75**, 1 (2002).
- [16] T. Hayashi, T. Fujisawa, H. D. Cheong, Y. H. Jeong, and Y. Hirayama, *Phys. Rev. Lett.* **91**, 226804 (2003).
- [17] J. R. Petta, A. C. Johnson, J. M. Taylor, E. A. Laird, A. Yacoby, M. D. Lukin, C. M. Marcus, M. P. Hanson, and A. C. Gossard, *Science* **309**, 2180 (2005).
- [18] C. Gould, A. S. Sachrajda, M. W. C. Dharma-wardana, Y. Feng, and P. T. Coleridge, *Phys. Rev. Lett.* **77**, 5272 (1996).
- [19] I. J. Maasilta and V. J. Goldman, *Phys. Rev. Lett.* **84**, 1776 (2000).
- [20] Z. F. Ezawa, *Quantum Hall Effects: Recent Theoretical and Experimental Developments* (World Scientific, Singapore, 2013).
- [21] T. Takakura, A. Noiri, T. Obata, T. Otsuka, J. Yoneda, K. Yoshida, and S. Tarucha, *Appl. Phys. Lett.* **104**, 113109 (2014).
- [22] F. R. Waugh, M. J. Berry, D. J. Mar, R. M. Westervelt, K. L. Campman, and A. C. Gossard, *Phys. Rev. Lett.* **75**, 705 (1995).
- [23] K. Grove-Rasmussen, H. I. Jørgensen, T. Hayashi, P. E. Lindelof, and T. Fujisawa, *Nano Lett.* **8**, 1055 (2008).
- [24] R. Eguchi, E. Kamata, C. Lin, H. Aramaki, and T. Fujisawa, *Appl. Phys. Express* **12**, 065002 (2019).
- [25] T. Hata, T. Uchino, T. Akiho, K. Muraki, and T. Fujisawa, *Jpn. J. Appl. Phys.* **59**, SGGI03 (2020).
- [26] A. Kou, C. M. Marcus, L. N. Pfeiffer, and K. W. West, *Phys. Rev. Lett.* **108**, 256803 (2012).
- [27] L. Gaudreau, S. A. Studenikin, A. S. Sachrajda, P. Zawadzki, A. Kam, J. Lapointe, M. Korkusinski, and P. Hawrylak, *Phys. Rev. Lett.* **97**, 036807 (2006).
- [28] D. Schröer, A. D. Greentree, L. Gaudreau, K. Eberl, L. C. L. Hollenberg, J. P. Kotthaus, and S. Ludwig, *Phys. Rev. B* **76**, 075306 (2007).
- [29] T. Takakura, M. Pioro-Ladrière, T. Obata, Y.-S. Shin, R. Brunner, K. Yoshida, T. Taniyama, and S. Tarucha, *Appl. Phys. Lett.* **97**, 212104 (2010).
- [30] M. Busl, G. Granger, L. Gaudreau, R. Sánchez, A. Kam, M. Pioro-Ladrière, S. A. Studenikin, P. Zawadzki, Z. R. Wasilewski, A. S. Sachrajda *et al.*, *Nat. Nanotechnol.* **8**, 261 (2013).
- [31] F. R. Braakman, P. Barthelemy, C. Reichl, W. Wegscheider, and L. M. Vandersypen, *Nat. Nanotechnol.* **8**, 432 (2013).
- [32] A. Noiri, T. Takakura, T. Obata, T. Otsuka, T. Nakajima, J. Yoneda, and S. Tarucha, *Phys. Rev. B* **96**, 155414 (2017).
- [33] J.-Y. Wang, S. Huang, G.-Y. Huang, D. Pan, J. Zhao, and H. Q. Xu, *Nano Lett.* **17**, 4158 (2017).
- [34] M. Kataoka, C. J. B. Ford, G. Faini, D. Mailly, M. Y. Simmons, and D. A. Ritchie, *Phys. Rev. B* **62**, R4817 (2000).
- [35] T. Fujisawa, G. Shinkai, T. Hayashi, and T. Ota, *Physica E* **43**, 730 (2011).